RSC Advances

PAPER

View Article Online
View Journal | View Issue

Cite this: *RSC Adv.*, 2025, **15**, 39909

Enhanced visible-light photocatalytic degradation of methylene blue *via* a ternary $Ag_2O@CuFe_2O_4@g\text{-}C_3N_4$ Z-scheme heterojunction with synergistic Fenton-like reactivity for sustainable water remediation

Huihui Fang,[a] Jianhua Wang *[ab] and Shuhui Shi[c]

The rational design of heterostructured photocatalysts is critical for addressing organic dye pollution through solar-driven advanced oxidation processes. Herein, a ternary $Ag_2O@CuFe_2O_4@g\text{-}C_3N_4$ nanocomposite was synthesized *via* a hydrothermal-precipitation route, integrating Z-scheme charge transfer and Fenton-like reactivity for enhanced visible-light photocatalysis. The composite's activity was evaluated *via* methylene blue (MB) degradation under a 300 W metal-halide lamp ($\lambda \geq 420$ nm), achieving 99.93% removal within 35 min—2.1× and 1.4× faster than pristine g-C_3N_4 and binary counterparts, respectively. This performance stems from synergistic effects: (i) a Z-scheme heterojunction between Ag_2O, $CuFe_2O_4$, and g-C_3N_4, which spatially separates electron–hole pairs *via* tailored band alignment; (ii) Fenton-like Fe^{3+}/Cu^{2+} redox cycles amplifying hydroxyl radical ($^{\bullet}OH$) generation; and (iii) uniform dispersion of Ag_2O and $CuFe_2O_4$ on g-C_3N_4 nanosheets, maximizing active sites. Radical trapping confirmed $^{\bullet}OH$ as the dominant species, with supplementary roles of h^+ and $^{\bullet}O_2^-$. The composite retained >93% activity over ten cycles, demonstrating robust stability due to interfacial coupling and inhibited agglomeration. This work advances the development of multifunctional heterostructures for sustainable water remediation, bridging photocatalysis and Fenton chemistry.

Received 25th April 2025
Accepted 15th October 2025

DOI: 10.1039/d5ra02882e

rsc.li/rsc-advances

Introduction

The rapid global industrial expansion, coupled with the escalating use of antibiotics, pesticides, and organic dyes, has intensified the contamination of freshwater resources, exacerbating the energy and water crisis.[1] Organic pollutants such as synthetic dyes, pharmaceutical metabolites, and pesticide residues—many of which contain carcinogenic heterocyclic aromatic or azo groups—pose severe threats to ecosystems and human health due to their persistence, toxicity, and resistance to conventional physical or chemical degradation methods.[2] Addressing these challenges necessitates advanced oxidation processes (AOPs) capable of efficiently degrading recalcitrant organic compounds. Among these, visible-light-driven photocatalysis has emerged as a sustainable solution, leveraging solar energy to activate catalytic materials for pollutant degradation and hydrogen production.[3]

While titanium dioxide (TiO_2) has been widely studied for photocatalysis, its large bandgap (~3.2 eV) restricts light absorption to the ultraviolet range (~5% of solar energy), limiting practical applications.[4] To overcome this, narrow-bandgap semiconductors such as ferrites and graphitic carbon nitride (g-C_3N_4) have gained attention. Spinel ferrites like $CuFe_2O_4$ exhibit structural stability, visible-light absorption, and magnetic recoverability, enabling their dual role as photomagnetic Fenton catalysts.[5] However, single-phase $CuFe_2O_4$ suffers from rapid charge recombination, low quantum yield, and limited surface area, hindering its photocatalytic efficiency.[6] Similarly, g-C_3N_4—a metal-free polymer with a moderate bandgap (~2.7 eV)—shows promise for visible-light-driven water splitting and pollutant degradation but is plagued by fast electron–hole (e^-–h^+) recombination.[7]

To address these limitations, heterostructured composites combining multiple semiconductors have been proposed. For instance, coupling g-C_3N_4 with $CuFe_2O_4$ enhances charge separation *via* Z-scheme mechanisms while enabling magnetic recovery.[8] Further improvements can be achieved by integrating silver oxide (Ag_2O), a p-type semiconductor with a narrow bandgap (~1.2 eV), which extends light absorption into the visible spectrum and promotes reactive oxygen species (ROS) generation (*e.g.*, $^{\bullet}OH$) through its redox-active surface.[9] The

[a]*Shenyang University, College of Science, Shenyang 110044, China. E-mail: jhwang1228@163.com*

[b]*Liaoning Provincial Key Laboratory of Micro–nano Materials Research and Development, Shenyang 110044, China*

[c]*Shenyang Institute of Engineering, College of Science, Shenyang 110136, China*

formation of p–n heterojunctions between Ag_2O, $CuFe_2O_4$, and g-C_3N_4 can synergistically suppress e^-–h^+ recombination, enhance charge transfer, and increase active sites for catalytic reactions.[10]

Herein, we design a ternary Ag_2O@$CuFe_2O_4$@g-C_3N_4 heterostructure to synergize the advantages of its components: (i) the visible-light responsiveness and porosity of g-C_3N_4, (ii) the magnetic Fenton activity of $CuFe_2O_4$, and (iii) the narrow-bandgap sensitization of Ag_2O. The composite's performance is evaluated *via* methylene blue (MB) degradation under visible light, demonstrating enhanced efficiency through interfacial charge transfer and ROS generation. Mechanistic studies reveal a dual Z-scheme pathway facilitated by band alignment, while the magnetic properties of $CuFe_2O_4$ ensure facile catalyst recovery. This work provides a scalable strategy for designing multifunctional photocatalysts to address water pollution, with potential applications in energy conversion and environmental remediation.

Experimental

Synthesis of g-C_3N_4

Graphitic carbon nitride (g-C_3N_4) was synthesized *via* thermal polycondensation using urea (CH_4N_2O, ≥99.0%, Sigma-Aldrich) and melamine ($C_3H_6N_6$, ≥99.0%, Alfa Aesar) as precursors. Both reagents were of analytical grade and used without further purification.[11–13] Urea and melamine were mixed in a 2 : 1 molar ratio and homogenized by grinding in an agate mortar for 30 min to ensure intimate contact between precursors. The homogeneous mixture was transferred to a covered alumina crucible and subjected to pyrolysis in a muffle furnace under static air. The temperature was ramped to 823 K at a heating rate of 2 K min^{-1}, maintained isothermally for 4 h to facilitate complete polycondensation, and then cooled naturally to ambient temperature. The resulting light-yellow bulk g-C_3N_4 was manually milled into a fine powder using an agate mortar, yielding a porous, layered structure.

Synthesis of Ag_2O@$CuFe_2O_4$@g-C_3N_4

The ternary Ag_2O@$CuFe_2O_4$@g-C_3N_4 composites were synthesized *via* a sequential hydrothermal and precipitation protocol, adapted from literature with modifications.[11–13]

Preparation of g-C_3N_4 dispersion (Solution A). Pre-synthesized g-C_3N_4 (0.05 g) was dispersed in 60 mL ethylene glycol ($C_2H_6O_2$, ≥99.8%, Sigma-Aldrich) *via* ultrasonication (40 kHz, 30 min) to achieve a homogeneous suspension.

Precursor mixing (Solution B). In a light-shielded environment (<5 lux) stoichiometric amounts of $FeCl_3 \cdot 6H_2O$, and $Cu(CH_3COO)_2 \cdot H_2O$ were dissolved in 25 mL deionized water. The molar ratio of Fe : Cu was fixed at 2 : 1. To obtain the ternary Ag_2O@$CuFe_2O_4$@g-C_3N_4 composites, $AgNO_3$ was loaded varied at 0–4 wt% relative to g-C_3N_4, $FeCl_3 \cdot 6H_2O$, and $Cu(CH_3COO)_2 \cdot H_2O$ (see Table 1).

Hydrothermal assembly. Solution B was gradually added to Solution A under magnetic stirring (500 rpm, 30 min), followed by the addition of 1 g urea (CH_4N_2O, ≥99.0%) and sodium citrate ($Na_3C_6H_5O_7$, ≥99.0%) in a 1 : 1 mass ratio. The mixture was stirred vigorously to ensure precursor homogeneity, then transferred into a 100 mL Teflon-lined stainless-steel autoclave. Hydrothermal treatment was conducted at 453 K for 12 h under autogenous pressure.

Post-synthesis processing. The cooled product was centrifuged (5000 rpm, 10 min) and washed sequentially with deionized water and absolute ethanol (C_2H_5OH, ≥99.9%) to remove unreacted ions. The resulting Ag_2O@$CuFe_2O_4$@g-C_3N_4 powder was dried in a vacuum oven (333 K, 12 h) to minimize aggregation.

Characterization

The structural and optical properties of the Ag_2O@$CuFe_2O_4$@g-C_3N_4 composites were systematically characterized. X-ray diffraction (XRD) patterns were acquired using a Rigaku Ultima IV diffractometer (Cu-Kα radiation, $\lambda = 1.5418$ Å, 40 kV, 40 mA) over a 2θ range of 10–80° to identify crystalline phases. Chemical states and surface composition were analyzed *via* X-ray photoelectron spectroscopy (XPS, Thermo Scientific K-Alpha) with Al-Kα excitation (1486.6 eV), and binding energies were calibrated against the C 1s peak (284.8 eV). In this study, a Thermo Scientific K-Alpha X-ray photoelectron spectrometer was used for testing. Strict adherence to the instrument's standard calibration specifications was maintained before and during the test to ensure data accuracy. The Ag_2O@$CuFe_2O_4$@g-C_3N_4 composite in this study has a semiconductor-polymer heterostructure, and the sample surface was prone to positive charge accumulation due to photoelectron emission, leading to

Table 1 The feeding ratio of Ag_2O@$CuFe_2O_4$@g-C_3N_4 composites

	g-C_3N_4/g	$FeCl_3$/g	$Cu(AC)_2$/g	$AgNO_3$/g	Sodium citrate and urea/g	Water/ml	Ethylene glycol/ml
Ag_2O@g-C_3N_4	0.050	0.00	0.00	0.005	1.00	25	60
$CuFe_2O_4$@g-C_3N_4	0.050	0.012	0.05	0.00	1.00	25	60
Ag_2O@$CuFe_2O_4$@g-C_3N_4-0	0.050	0.00	0.00	0.00	1.00	25	60
Ag_2O@$CuFe_2O_4$@g-C_3N_4-1	0.050	0.028	0.014	0.0008	1.00	25	60
Ag_2O@$CuFe_2O_4$@g-C_3N_4-2	0.050	0.028	0.014	0.0016	1.00	25	60
Ag_2O@$CuFe_2O_4$@g-C_3N_4-3	0.050	0.028	0.014	0.0021	1.00	25	60
Ag_2O@$CuFe_2O_4$@g-C_3N_4-4	0.050	0.028	0.014	0.0029	1.00	25	60

a shift in the binding energy peak position. To eliminate the charge effect, we adopted a composite charge compensation strategy of "low-energy electron neutralization gun + sample grounding", with the specific operations. Morphological features, including particle dispersion and heterojunction interfaces, were examined by field-emission scanning electron microscopy (FE-SEM, Hitachi SU8010) and high-resolution transmission electron microscopy (HR-TEM, JEOL JEM-2100F) operated at 200 kV. Optical absorption spectra were recorded using a PerkinElmer LAMBDA750 UV-Vis-NIR spectrophotometer equipped with a diffuse reflectance accessory (DRS, 200–800 nm), and bandgap energies were derived from Tauc plots using the Kubelka–Munk function. Photoluminescence (PL) spectra were measured at room temperature with a Horiba Fluorolog-3 spectrofluorometer (excitation λ = 380 nm) to assess charge carrier recombination dynamics.

Photocatalytic performance was evaluated by monitoring methylene blue (MB) degradation under visible light (300 W Xe lamp, $\lambda \geq 420$ nm), with absorbance at 664 nm tracked using a Shimadzu UV-2600 spectrophotometer. Reaction kinetics were modeled using the pseudo-first-order rate equation $-\ln(C/C_0) = kt$, where k is the rate constant. For degradation cycle, the catalyst was separated from the MB solution using high speed centrifugation method—this method avoids catalyst loss compared to magnetic separation and ensures high recovery efficiency (>98%). The recovered catalyst was sequentially washed with deionized water and absolute ethanol to remove residual MB molecules or intermediate products adsorbed on the surface, then dried in a vacuum oven at 333 K for 2 h to restore its dry state. For each subsequent cycle, a fresh MB solution (100 mL, 30 mg L^{-1}) was prepared, and the regenerated catalyst (0.05 g) was re-dispersed into the solution. The adsorption–desorption equilibrium step (dark stirring for 60 min) and irradiation conditions (lamp power, distance from reaction vessel) were strictly identical to the first cycle.

Photocatalytic activity

The photocatalytic performance of the Ag_2O@$CuFe_2O_4$@g-C_3N_4 composites was evaluated by degrading methylene blue (MB) under visible-light irradiation. A 300 W metal-halide lamp (Philips, $\lambda \geq 420$ nm with a UV cutoff filter) served as the light source, positioned 20 cm above the reaction vessel. Prior to illumination, 0.05 g of catalyst was dispersed in 100 mL of MB solution (30 mg L^{-1}) and magnetically stirred in the dark for 60 min to establish adsorption–desorption equilibrium. During irradiation, 3 mL aliquots were extracted at 10 min intervals, centrifuged (8000 rpm, 5 min) to remove catalyst particles, and analyzed using a UV-Vis spectrophotometer (Shimadzu UV-2600) by monitoring the absorbance at 664 nm. The degradation efficiency (η) and pseudo-first-order rate constant (k) were calculated as:

$$\eta\ (\%) = (1 - C_t/C_0) \times 100,\ \ln(C_t/C_0) = kt \quad (1)$$

where C_0 and C_t represent the initial and time-dependent MB concentrations, respectively.

To identify reactive species, radical trapping experiments were conducted by introducing 1 mM scavengers: isopropanol (IPA, $^{\cdot}OH$ quencher), ethylenediaminetetraacetic acid (EDTA, h^+ quencher), and benzoquinone (BQ, $^{\cdot}O_2^-$ quencher). Control experiments without catalysts or light were performed to confirm the absence of non-photocatalytic degradation.

Results and discussion

X-ray diffraction analysis

The crystallographic phases of the synthesized materials were characterized by X-ray diffraction (XRD). As shown in Fig. 1a, pristine g-C_3N_4 exhibits a distinct peak at 27.8°, corresponding to the (002) interlayer stacking plane of graphitic carbon nitride (JCPDS 87-1526).[14] For the Ag_2O@g-C_3N_4 composite (Fig. 1b), diffraction peaks at 38.0°, 44.2°, 64.5°, and 77.3° are indexed to the (200), (220), (311), and (222) planes of cubic-phase Ag_2O (JCPDS 41-1104), confirming its successful integration.[15] Similarly, $CuFe_2O_4$@g-C_3N_4 (Fig. 1c) displays peaks at 24.18°, 33.08°, 35.9°, 40.9°, 43.64°, 49.68°, 54.22°, 57.68°, 62.46°, 64.22°, 71.98°, and 75.64°, which align with the (012), (104), (110), (113), (202), (024), (116), (122), (214), (300), (1010), and (220) planes of tetragonal spinel $CuFe_2O_4$ (JCPDS 34-0425).[16]

For the ternary Ag_2O@$CuFe_2O_4$@g-C_3N_4 composite (Fig. 1d, blue curve), the characteristic peaks of Ag_2O (38.0° for (200), 44.2° for (220), JCPDS 41-1104) and $CuFe_2O_4$ (35.9° for (110), 40.9° for (113), JCPDS 34-0425) are clearly observed alongside the (002) peak of g-C_3N_4 (27.8°). The absence of impurity peaks (*e.g.*, α-Fe_2O_3 at 33.2°, CuO at 35.5°) indicates that the hydrothermal-precipitation process successfully synthesizes pure Ag_2O and $CuFe_2O_4$, which are uniformly loaded onto the g-C_3N_4 matrix without secondary phase formation. This further confirms the successful construction of the ternary heterostructure, as the intrinsic crystalline phases of all components are retained.

To evaluate the effect of $Ag_2O/CuFe_2O_4$ loading on the crystalline structure of g-C_3N_4, the full width at half maximum (FWHM) of the (002) peak was compared across all samples. The FWHM of the (002) peak in pure g-C_3N_4 is 2.19°; in Ag_2O@g-C_3N_4 and $CuFe_2O_4$@g-C_3N_4, it slightly decreases to 1.14° and 1.36°, respectively. For the ternary composite, the FWHM of the (002) peak is 0.76°, which is marginally narrowed than that of

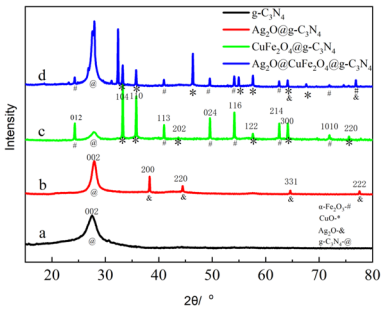

Fig. 1 XRD patterns of (a) g-C_3N_4, (b) Ag_2O@g-C_3N_4, (c) $CuFe_2O_4$@g-C_3N_4 and (d) Ag_2O@$CuFe_2O_4$@g-C_3N_4.

pure g-C_3N_4 but without significant broadening. Crystallite sizes were calculated using the Scherrer equation:

$$D = \beta \cos \theta k\lambda \quad (2)$$

where D is the crystallite diameter, $k = 0.89$ (shape factor), $\lambda = 1.5418$ Å (Cu-Kα wavelength), β is the full width at half maximum (FWHM), and θ is the Bragg angle. According to the Scherrer equation, the crystallite size of g-C_3N_4 in the ternary composite is calculated to be 10.5 nm, comparable to that of pure g-C_3N_4 (26.5 nm). This minor FWHM variation may arise from the interfacial interaction between g-C_3N_4 and the loaded $Ag_2O/CuFe_2O_4$ nanoparticles, but it does not indicate obvious lattice distortion or crystallinity degradation of g-C_3N_4. This result is consistent with the earlier conclusion that the heterostructure synthesis preserves the intrinsic crystallinity of each component, which is critical for maintaining efficient charge transfer at the interfaces. Based on the dominant (200) and (113) peaks, Ag_2O and $CuFe_2O_4$ crystallites averaged 51.44 ± 1.2 nm and 48.14 ± 0.9 nm, respectively, confirming nanoscale dimensions (Fig. 1d).

Morphological and structural characterization (SEM/TEM)

The microstructural evolution of the synthesized composites was systematically investigated using scanning and transmission electron microscopy. With the unified scale in Fig. 2, the following features are more clearly comparable: (1) pristine g-C_3N_4 exhibits curled lamellar nanosheets with a lateral size of 1–2 μm, consistent with its layered graphitic structure; (2) Ag_2O nanoparticles (35–45 nm) in Ag_2O@g-C_3N_4 are uniformly dispersed on the g-C_3N_4 nanosheets without obvious agglomeration; (3) $CuFe_2O_4$ particles (50–85 nm) in $CuFe_2O_4$@g-C_3N_4 are embedded in the interlayer gaps of g-C_3N_4, with a slightly larger particle size than Ag_2O; (4) in the ternary composite, Ag_2O (40 ± 5 nm) and $CuFe_2O_4$ (60 ± 8 nm) nanoparticles maintain heterogeneous distribution on g-C_3N_4 nanosheets, with no significant change in the lamellar structure of g-C_3N_4 compared to the pristine sample. This unified scale not only clarifies the morphological evolution of the composite system but also confirms the effective interfacial coupling between each component during synthesis. This competitive nucleation and growth process, coupled with the surface energy heterogeneity of g-C_3N_4, directly results in the observed selective attachment of Ag_2O and $CuFe_2O_4$, which further supports the formation of a well-dispersed ternary heterostructure.

High-resolution TEM (Fig. 3) provides crystallographic validation of the heterostructure. Pristine g-C_3N_4 (Fig. 3a) shows amorphous domains interspersed with ordered lattice fringes, consistent with its (002) interlayer stacking. In Ag_2O@g-C_3N_4 (Fig. 3b), discrete Ag_2O nanoparticles (30–50 nm) are anchored to the g-C_3N_4 surface. $CuFe_2O_4$@g-C_3N_4 (Fig. 3c) reveals tetragonal $CuFe_2O_4$ particles (50–85 nm) are anchored to the g-C_3N_4 surface.

For the ternary composite (Fig. 3d), cubic-phase Ag_2O and tetragonal $CuFe_2O_4$ nanoparticles (20–50 nm) are co-located on g-C_3N_4 nanosheets, forming intimate heterojunctions. The distinct lattice fringes (Ag_2O: 0.2372 nm (2 0 0), AgO: 0.2287 nm (2 0 1), 0.2236 nm(1 1 1), $CuFe_2O_4$: 0.219 nm (4 0 0)) and absence of interfacial amorphous layers confirm crystallographic coherence, critical for efficient charge transfer.

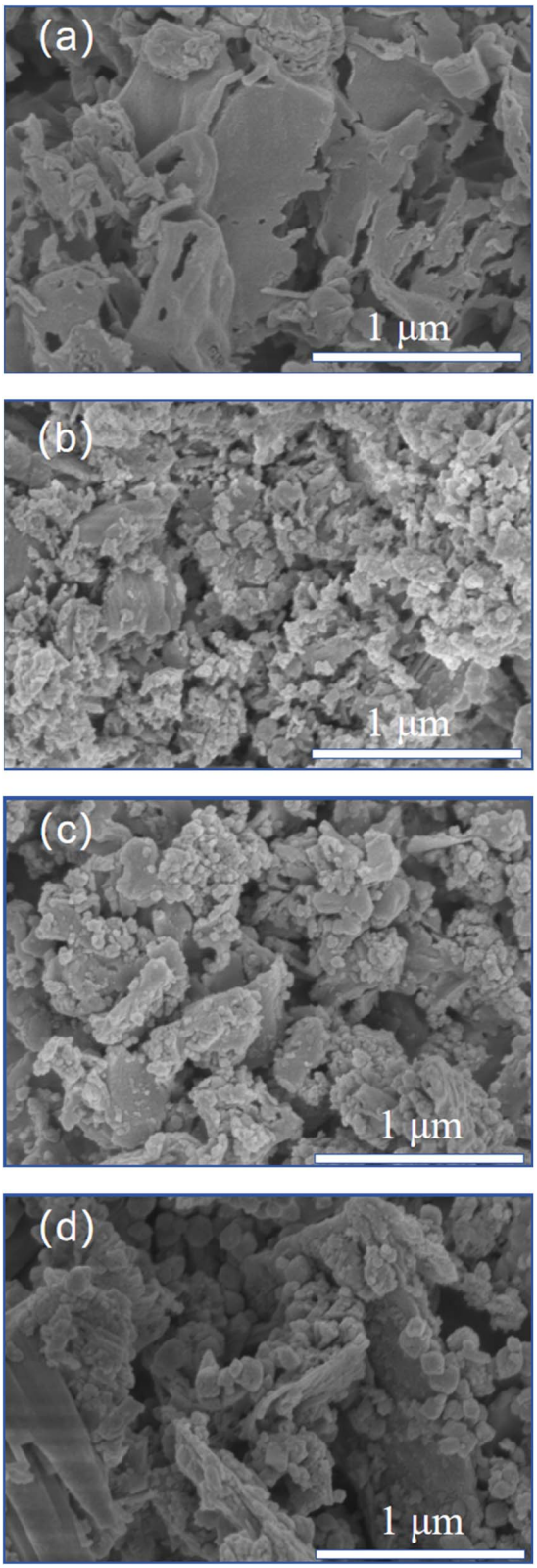

Fig. 2 SEM images of (a) g-C_3N_4, (b) Ag_2O@g-C_3N_4, (c) $CuFe_2O_4$@g-C_3N_4 and (d) Ag_2O@$CuFe_2O_4$@g-C_3N_4.

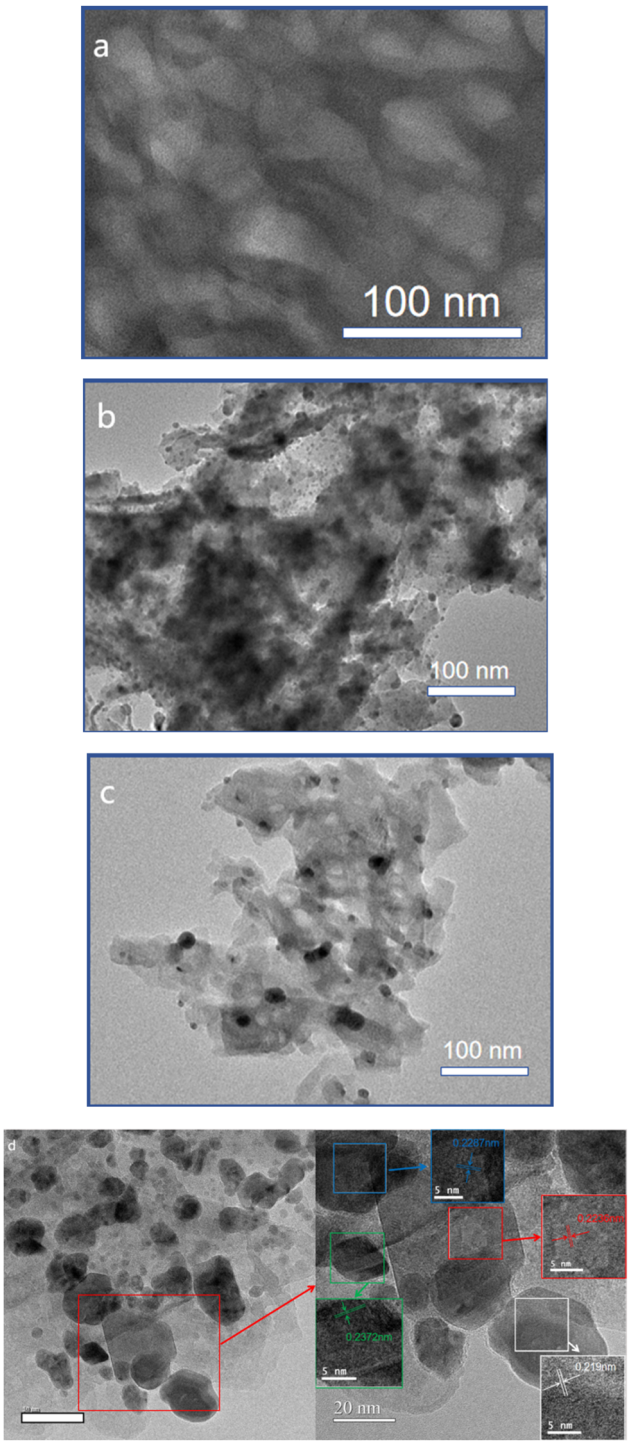

Fig. 3 TEM images of (a) g-C_3N_4, (b) Ag_2O@g-C_3N_4, (c) $CuFe_2O_4$@g-C_3N_4 and (d) Ag_2O@$CuFe_2O_4$@g-C_3N_4.

XPS analysis

X-ray photoelectron spectroscopy (XPS) was employed to probe the chemical states and surface composition of the Ag_2O@$CuFe_2O_4$@g-C_3N_4 heterostructure (Fig. 4a). The survey spectrum confirms the presence of C, O, N, Ag, Fe, and Cu, corroborating the successful integration of Ag_2O and $CuFe_2O_4$ into the g-C_3N_4 matrix (Yao *et al.*, 2015). High-resolution Ag 3d

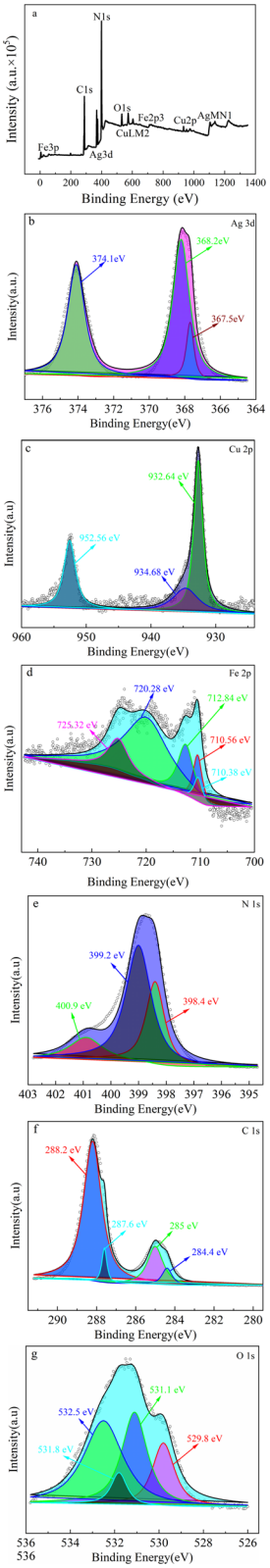

Fig. 4 XPS analysis of Ag_2O@$CuFe_2O_4$@g-C_3N_4 heterojunction emerging from the emissions of the Ag, Cu, Fe, N, C, and O elements; (a) survey spectrum of Ag_2O@$CuFe_2O_4$@g-C_3N_4, (b) Ag 3d, (c) Cu 2p, (d) Fe 2p, (e) N 1s, (f) C 1s and (g) O 1s.

spectra (Fig. 4b) and $\Delta E = E_3d_{3/2} - E_3d_{5/2} \approx 6.0$ eV reveal peaks at 368.3 eV (Ag $3d_{5/2}$) and 374.3 eV (Ag $3d_{3/2}$), deconvoluted into three components at 367.5 eV (Ag^0), 368.2 eV (Ag^+ in Ag_2O), and 374.1 eV (Ag^{2+} in AgO), indicating partial oxidation. The Cu 2p spectrum (Fig. 4c) displays peaks at 932.4 eV (Cu $2p_{3/2}$) and 952.2 eV (Cu $2p_{1/2}$), resolved into Cu^+ (932.64 eV) and Cu^{2+} (934.68 eV), confirming Cu_2O and CuO coexistence. Similarly, the Fe $2p_{3/2}$ peak resolves into contributions at 710.38 eV, 710.56 eV (Fe^{2+} in FeO) and 712.84 eV (Fe^{3+} in Fe_2O_3), while Fe $2p_{1/2}$ peaks at 725.32 eV and 720.28 eV further validate mixed Fe oxidation states. N 1s spectra (Fig. 4e) resolve into three peaks at 398.4 eV (C=N–C), 399.2 eV (N–$(C)_3$), and 400.9 eV (C–N–H), characteristic of g-C_3N_4's triazine structure. C 1s signals (Fig. 4f) at 284.4 eV (C–C), 285.0 eV (C–O/N), 287.6 eV (sp^2 C in g-C_3N_4), and 288.2 eV (O–C=O) reflect graphitic and functionalized carbon. O 1s deconvolution (Fig. 4g) identifies contributions from lattice oxygen in $CuO/Ag_2O/Fe_2O_3$ (529.7–531.1 eV), surface hydroxyl groups (531.8 eV), and adsorbed H_2O (532.5 eV). Collectively, the XPS data confirm the coexistence of $Ag^0/Ag^+/Ag^{2+}$, Cu^+/Cu^{2+}, and Fe^{2+}/Fe^{3+} redox pairs, anchored as Ag_2O, Cu_2O/CuO, and FeO/Fe_2O_3 on g-C_3N_4 nanosheets. Combined with TEM evidence, this confirms the formation of a multifunctional heterostructure with interfacial charge-transfer pathways, critical for visible-light-driven photocatalytic activity.

Optical properties

The light-harvesting capabilities and charge-carrier dynamics of the synthesized materials were investigated through UV-Vis diffuse reflectance spectroscopy (DRS) and photoluminescence (PL) spectroscopy. As shown in Fig. 5a, the $Ag_2O@CuFe_2O_4@g$-C_3N_4 heterostructure exhibits a pronounced red shift in absorption edge and enhanced visible-light absorption compared to pristine g-C_3N_4, attributed to synergistic interactions between the constituent phases. The optical bandgap energies (E_g), calculated *via* Tauc plots (Fig. 5b), decrease sequentially from 2.74 eV (g-C_3N_4) to 1.82 eV (ternary composite), confirming extended light absorption into the visible-NIR range. This broadening aligns with the formation of a p–n heterojunction, which enhances solar energy utilization by minimizing charge recombination. PL spectra (Fig. 5c) further reveal a marked quenching of emission intensity in the heterostructure, signifying suppressed electron–hole recombination due to efficient interfacial charge transfer between Ag_2O, $CuFe_2O_4$, and g-C_3N_4. These findings collectively demonstrate that the heterostructure design optimizes both light absorption and charge separation, critical for high-performance photocatalysis under visible irradiation.

As shown in Fig. 5, the interfacial charge transfer and separation of the $Ag_2O@CuFe_2O_4@g$-C_3N_4 ternary composite follow a dual Z-scheme heterojunction mechanism, whose thermodynamic feasibility and kinetic processes are jointly verified by band alignment, charge migration pathways, and experimental characterizations. Firstly, the band structures of the three components were determined *via* UV-Vis diffuse reflectance spectroscopy (Fig. 5) and X-ray photoelectron

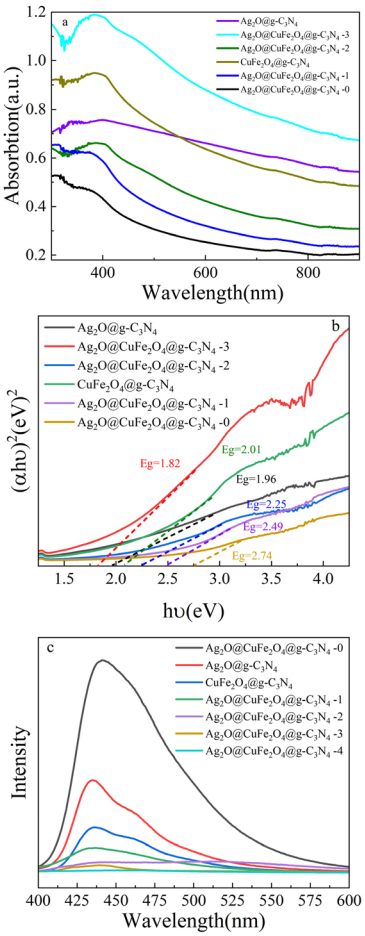

Fig. 5 (a) Diffuse reflectance spectra of $Ag_2O@g$-C_3N_4, $CuFe_2O_4@g$-C_3N_4 and $Ag_2O@CuFe_2O_4@g$-C_3N_4; (b) plot of transferred Kubelka–Munk *versus* the energy of the light absorbed for of $Ag_2O@g$-C_3N_4, $CuFe_2O_4@g$-C_3N_4 and $Ag_2O@CuFe_2O_4@g$-C_3N_4; (c) PL spectra of $Ag_2O@g$-C_3N_4, $CuFe_2O_4@g$-C_3N_4 and $Ag_2O@CuFe_2O_4@g$-C_3N_4.

spectroscopy (Fig. 4) valence band (VB) spectra:[2,7] for g-C_3N_4, the optical bandgap (E_g) is 2.74 eV, the VB potential (E_{VB}) is +2.46 eV *vs.* normal hydrogen electrode (NHE), and the conduction band (CB) potential (E_{CB}) is −0.43 eV; for $CuFe_2O_4$, $E_g = 1.42$ eV, $E_{VB} =$ +0.21 eV, and $E_{CB} = -1.21$ eV; for Ag_2O, $E_g = 1.20$ eV, $E_{VB} =$ +1.35 eV, and $E_{CB} = +0.15$ eV. This band alignment satisfies the thermodynamic requirements for a dual Z-scheme heterojunction. The CB potential of g-C_3N_4 (−0.43 eV) is more negative than the VB potential of $CuFe_2O_4$ (+1.42 eV), which enables photogenerated electrons in the CB of g-C_3N_4 to transfer to the VB of $CuFe_2O_4$ and recombine with holes; the CB potential of Ag_2O (+0.15 eV) is more positive than the VB potential of g-C_3N_4, driving electrons in the CB of Ag_2O to migrate to the VB of g-C_3N_4 and recombine with holes. In contrast, the traditional type-II heterojunction is thermodynamically disadvantageous, as the CB of Ag_2O cannot reduce O_2 to $^{\bullet}O_2^-$ and the VB of $CuFe_2O_4$ cannot oxidize H_2O to $^{\bullet}OH$. Therefore, the dual Z-scheme structure is the only effective configuration for retaining redox-active electron–hole pairs.

Under visible-light irradiation, the charge transfer process proceeds in three steps. In the charge generation step, g-C_3N_4

and Ag_2O absorb visible light to generate electron–hole pairs, while $CuFe_2O_4$ only produces a small number of electron–hole pairs due to weak visible-light absorption. In the Z-scheme charge transfer step (mediated by Ag^0), in the first Z-scheme pathway, electrons in the CB of g-C_3N_4 migrate to the VB of $CuFe_2O_4$ and recombine with holes; XPS results show an increased content of Fe^{2+} (at 710.38 eV) in the ternary composite, confirming that electron injection into $CuFe_2O_4$ triggers the conversion of Fe^{3+} to Fe^{2+}, while retaining holes at +1.4 eV in the VB of g-C_3N_4 and electrons at −1.28 eV in the CB of $CuFe_2O_4$. In the second Z-scheme pathway, electrons in the CB of Ag_2O cannot directly transfer to the VB of g-C_3N_4 due to an energy barrier; however, the partial reduction of Ag_2O to Ag^0 (XPS Ag $3d_{5/2}$ peak at 367.5 eV) forms an electron bridge, mediating electron transfer from the CB of Ag_2O to the VB of g-C_3N_4 *via* Ag^0 for recombination with holes, and retaining strongly oxidizing holes at +2.46 eV in the VB of Ag_2O and electrons at −1.34 eV in the CB of g-C_3N_4.

In the charge separation and reactive oxygen species (ROS) generation step, the retained electrons reduce O_2 to $^{\cdot}O_2^-$, and the retained holes oxidize H_2O/OH^- to $^{\cdot}OH$. Additionally, Fe^{2+}/Cu^+ in $CuFe_2O_4$ react with H_2O_2 (generated by the protonation of $^{\cdot}O_2^-$) through Fenton-like cycles, further enhancing $^{\cdot}OH$ generation. Moreover, photoluminescence spectroscopy (Fig. 5c) confirm that the dual Z-scheme structure not only achieves spatial separation of electrons and holes but also retains their strong redox capabilities, effectively addressing the key limitations of single/binary catalysts.

Photocatalytic performance

Recent advances in 2D heterostructures have further pushed the boundary of visible-light photocatalysis, as their ultra-thin planar structure provides large specific surface area and short charge-transfer paths.[17,18] These studies confirm the potential of 2D heterostructures but also highlight their limitations. To address these, we design a ternary $Ag_2O@CuFe_2O_4@$g-C_3N_4 2D heterostructure that integrates Z-scheme charge transfer and Fenton-like reactivity—filling the gap in multi-functional 2D heterostructure design. The visible-light-driven photocatalytic activity of the $Ag_2O@CuFe_2O_4@$g-C_3N_4 composites was evaluated through methylene blue (MB) degradation (30 mg L^{-1}) under irradiation from a 300 W metal-halide lamp ($\lambda \geq 420$ nm). Prior to illumination, 0.05 g of catalyst was dispersed in 100 mL of MB solution and magnetically stirred in the dark for 60 min to establish adsorption–desorption equilibrium. Aliquots (3 mL) were extracted at 5 min intervals, centrifuged to remove catalyst particles, and analyzed *via* UV-Vis spectrophotometry by monitoring the MB absorbance at 664 nm (Fig. 6a). Fig. 6a shows the time-dependent UV-Vis spectra of MB during degradation, where the characteristic peak of MB at 664 nm (attributed to the $\pi \rightarrow \pi^*$ transition of the conjugated chromophore in MB molecules) decreases significantly with irradiation time, indicating efficient decolorization. Notably, the minor absorption peak near 300 nm also depresses synchronously, and this peak is assigned to the $\pi \rightarrow \pi^*$ transition of the aromatic benzene/heterocyclic rings in the MB molecular skeleton. The

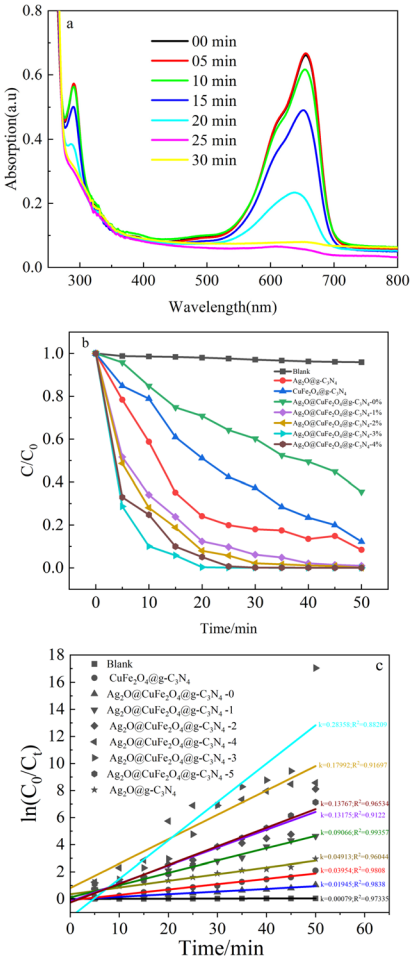

Fig. 6 The degradation curves of MB under visible lights change of (a) character peak, (b) degradation rate, (c) kinetic plots with irradiated time.

synchronous reduction of both peaks confirms that the $Ag_2O@CuFe_2O_4@$g-C_3N_4 catalyst not only breaks the conjugated chromophore (responsible for MB's blue color) but also degrades the aromatic/heterocyclic backbone of MB—avoiding the accumulation of toxic intermediate products with intact aromatic rings. This is further supported by the absence of new absorption peaks in the 250–400 nm range (Fig. 6a), which rules out the formation of stable intermediate species and confirms the thorough mineralization of MB.

As shown in Fig. 6b, the ternary $Ag_2O@CuFe_2O_4@$g-C_3N_4-3% composite achieved 99.94% MB degradation within 35 min, outperforming pristine g-C_3N_4 (47.55%), $Ag_2O@$g-C_3N_4 (82.41%), and $CuFe_2O_4@$g-C_3N_4 (71.56%). Control experiments confirmed negligible photolysis (<5%) in the absence of catalysts. The degradation kinetics followed pseudo-first-order behavior, with the ternary composite exhibiting a rate constant $k = 0.132$ min^{-1}, 2.10-, 1.21-, and 1.40-fold higher than g-C_3N_4, $Ag_2O@$g-C_3N_4, and $CuFe_2O_4@$g-C_3N_4, respectively. Notably, 90% MB degradation occurred within 17–20 min, highlighting rapid reaction kinetics (Fig. 6c). As shown in Fig. S1, the ternary $Ag_2O@CuFe_2O_4@$g-C_3N_4-3% have a better

Table 2 Comparison of catalytic efficiency of $Ag_2O@CuFe_2O_4@g\text{-}C_3N_4$ catalyst with previous literature for the reduction of MB

Organic dye	Catalyst	k_{app} (s^{-1})	Ref.
MB	$g\text{-}C_3N_4/NiFe_2O_4$ (1 g l^{-1}, r.t.)	7.33×10^{-3}	16
MB	NiO-$g\text{-}C_3N_4$ (0.5 g l^{-1}, r.t.)	8.33×10^{-3}	16
MB	$g\text{-}C_3N_4/ZnO$ (0.5 gl^{-1}, r.t.)	3.10×10^{-3}	16
MB	$CaFe_2O_4/g\text{-}C_3N_4$ (20 wt% $CaFe_2O_4$, 2 g l^{-1}, r.t.)	0.288×10^{-3}	16
MB	$g\text{-}C_3N_4$ quantum dots/ZnO nanosheets (0.125 g l^{-1}, r.t.)	0.855×10^{-3}	16
MB	Graphite carbon coating hollow $CuFe_2O_4$ spheres (0.1 g l^{-1}, r.t.)	0.633×10^{-3}	16
MB	$Ag_2O@CuFe_2O_4@g\text{-}C_3N_4$-1 (0.5 g l^{-1}, r.t.)	1.511×10^{-3}	This work
	$Ag_2O@CuFe_2O_4@g\text{-}C_3N_4$-2 (0.5 g l^{-1}, r.t.)	2.196×10^{-3}	
	$Ag_2O@CuFe_2O_4@g\text{-}C_3N_4$-3 (0.5 g l^{-1}, r.t.)	4.726×10^{-3}	
	$Ag_2O@CuFe_2O_4@g\text{-}C_3N_4$-4 (0.5 g l^{-1}, r.t.)	2.998×10^{-3}	
	$Ag_2O@CuFe_2O_4@g\text{-}C_3N_4$-5 (0.5 g l^{-1}, r.t.) time	2.295×10^{-3}	

catalysis performance than pristine Ag_2O, pristine $CuFe_2O_4$ and pristine $g\text{-}C_3N_4$.

Optimal performance was observed at a 3% $Ag_2O@CuFe_2O_4$ loading, where the heterojunction structure facilitated efficient charge separation while minimizing agglomeration. Increasing the loading to 4% reduced degradation efficiency to 99.91% due to particle aggregation, which restricted charge carrier mobility and increased electron–hole recombination. This underscores the critical balance between heterojunction density and dispersion: at 3% loading, uniformly distributed Ag_2O and $CuFe_2O_4$ nanoparticles on $g\text{-}C_3N_4$ nanosheets enhanced light absorption, active site availability, and interfacial charge transfer, whereas excessive loading (4%) disrupted these synergies. To highlight the advantages of the $Ag_2O@CuFe_2O_4@g\text{-}C_3N_4$ ternary composite, its MB degradation performance was compared with that of similar $g\text{-}C_3N_4$-based photocatalysts reported in recent literature (Table 2).[16]

As shown in Table 2, the ternary $Ag_2O@CuFe_2O_4@g\text{-}C_3N_4$ composite outperforms most literature-reported counterparts. Firstly, its rate constant 1.511×10^{-3} to 4.726×10^{-3} are higher than most $g\text{-}C_3N_4$ coupled catalyst; Secondly, it achieves nearly complete MB removal in 35 min, which higher than most $g\text{-}C_3N_4$ coupled catalyst under the same MB concentration and catalyst dosage; Finally, it retains >95% activity after 10 cycles, outperforming catalysts with fewer cycles or lower retention.

This enhanced performance originates from the synergistic effect of the Z-scheme heterojunction and Fenton-like reactivity, which addresses the limitations of single/binary catalysts reported in literature. These results confirm that $Ag_2O@CuFe_2O_4@g\text{-}C_3N_4$ is a competitive candidate for sustainable MB-contaminated water remediation.

The recyclability of the $Ag_2O@CuFe_2O_4@g\text{-}C_3N_4$ composite was evaluated *via* ten consecutive MB degradation cycles, following a standardized protocol to ensure consistent experimental conditions across cycles as description in Characterization. The recyclability of the $Ag_2O@CuFe_2O_4@g\text{-}C_3N_4$ composite was evaluated over ten consecutive photocatalytic cycles (Fig. 7). The material retained >95% of its initial degradation efficiency, with no significant decline in performance, demonstrating exceptional cyclic stability. This robust retention of activity underscores the structural integrity of the $Ag_2O@CuFe_2O_4@g\text{-}C_3N_4$ heterojunction, confirming that the interfacial coupling between Ag_2O, $CuFe_2O_4$, and $g\text{-}C_3N_4$ remains stable under prolonged photocatalytic operation.

Active species analysis

To elucidate the dominant reactive species governing the photocatalytic mechanism, radical trapping experiments were conducted using tert-butanol (TBA) as a hydroxyl radical ($^{\bullet}OH$) scavenger. Under visible-light irradiation (300 W metal-halide lamp, $\lambda \geq 420$ nm), the degradation of MB by $Ag_2O@CuFe_2O_4@g\text{-}C_3N_4$ was evaluated in the presence and absence of TBA (Fig. 8). The introduction of TBA drastically suppressed MB degradation, reducing efficiency from 99.93% to 26.68% within 25 min, confirming $^{\bullet}OH$ as the primary oxidative species. Notably, residual degradation in TBA-containing systems

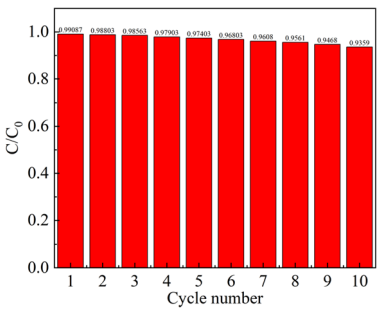

Fig. 7 Recycling test of MB using $Ag_2O@CuFe_2O_4@g\text{-}C_3N_4$ catalysts.

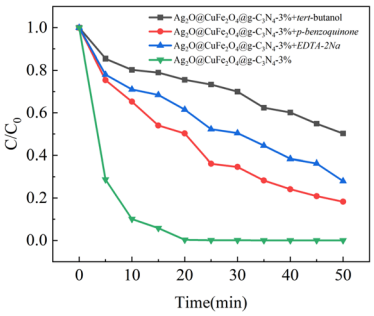

Fig. 8 Influences of different scavengers on photocatalytic degradation of MB in the presence of $Ag_2O@CuFe_2O_4@g\text{-}C_3N_4$-3 catalysts.

(Fig. 8) suggests minor contributions from alternate pathways (*e.g.*, direct h^+ oxidation or $^{\bullet}O_2^-$ participation). However, the near-complete quenching of activity underscores the pivotal role of $^{\bullet}OH$, generated *via* H_2O oxidation by photogenerated holes and Fenton-like reactions involving $CuFe_2O_4$. These results align with the heterostructure's band alignment, which facilitates spatially separated redox reactions, optimizing $^{\bullet}OH$ yield for rapid dye mineralization.

The reactive species generated during visible-light photocatalysis were systematically probed through radical trapping experiments. As depicted in Fig. 8, the degradation profiles of MB were compared across four systems: (i) pristine $Ag_2O@CuFe_2O_4@g\text{-}C_3N_4$, (ii) composite with *p*-benzoquinone (BQ, $^{\bullet}O_2^-$ scavenger), (iii) composite with tert-butanol (TBA, $^{\bullet}OH$ scavenger), and (iv) composite with disodium ethylenediaminetetraacetate dihydrate (EDTA-2Na, h^+ scavenger). Under 50 min of visible-light irradiation, the degradation efficiency declined from 98.06% (pristine catalyst) to 53.08% (BQ), 20.15% (TBA), and 38.60% (EDTA-2Na) within 20 min. This hierarchical suppression—most pronounced with TBA—confirmed hydroxyl radicals ($^{\bullet}OH$) as the dominant active species, with supplementary roles of superoxide radicals ($^{\bullet}O_2^-$) and holes (h^+). The results underscore a reaction mechanism where $^{\bullet}OH$, produced *via* H_2O oxidation by h^+ and Fenton-like Fe^{2+}/Cu^+ cycles, drives MB mineralization, while $^{\bullet}O_2^-$ and direct h^+ oxidation contribute secondary pathways.

Proposed activation mechanism

Fig. 9 schematically illustrates the Z-scheme charge transfer and photo-Fenton synergistic mechanism for MB degradation by $Ag_2O@CuFe_2O_4@g\text{-}C_3N_4$, with band positions of $g\text{-}C_3N_4$, $CuFe_2O_4$, and Ag_2O referenced to literature, the dual Z-scheme adapted from $g\text{-}C_3N_4$-based heterostructure principles, and photo-Fenton reactions ($Fe^{2+}/Cu^+ + H_2O_2 \rightarrow {}^{\bullet}OH + Fe^{3+}/Cu^{2+}$) aligning with $CuFe_2O_4$'s reported redox behavior. Based on discussed in interfacial charge transfer and separation[2,7,17,18] of the $Ag_2O@CuFe_2O_4@g\text{-}C_3N_4$ ternary composite. Under visible light ($\lambda \geq 420$ nm), three steps occur: (1) charge generation; (2) Z-scheme transfer; (3) retained e^- reduce O_2 to $^{\bullet}O_2^-$, retained h^+ oxidize OH^- to $^{\bullet}OH$. The equations in the Fig. 9 show photo-Fenton ROS amplification: $^{\bullet}O_2^-$ protonates to H_2O_2, $CuFe_2O_4$'s Fe^{3+}/Cu^{2+} reduce to Fe^{2+}/Cu^+, and $^{\bullet}OH/^{\bullet}O_2^-/h^+$ mineralize MB.

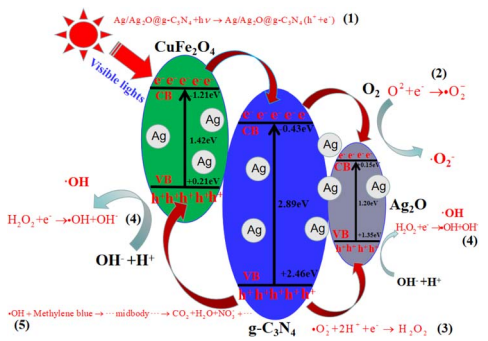

Fig. 9 Improvement photocatalytic oxidation of MB over $Ag_2O@CuFe_2O_4@g\text{-}C_3N_4$ heterostructures.

XPS, quenched PL, and TBA-suppressed efficiency validate the mechanism.

Conclusions

In this study, a highly efficient $Ag_2O@CuFe_2O_4@g\text{-}C_3N_4$ heterostructured composite was successfully synthesized, integrating Z-scheme charge transfer and Fenton-like reactivity for visible-light-driven organic dye degradation. Structural and compositional analyses confirmed the incorporation of Fe^{3+}, Cu^{2+}, and Cu^+ species into the $g\text{-}C_3N_4$ framework, while the introduction of Ag_2O and $CuFe_2O_4$ enhanced specific surface area and adsorption capacity for methylene blue (MB). The Z-scheme heterojunction, governed by the band alignment of Ag_2O (−0.5 eV CB), $CuFe_2O_4$ (+0.7 eV VB), and $g\text{-}C_3N_4$ (−1.3 eV CB/+1.4 eV VB), facilitated spatial separation of photogenerated electron–hole pairs, suppressing recombination and prolonging carrier lifetimes. Recyclability tests demonstrated exceptional stability, with >95% MB degradation retained over ten cycles, underscoring the catalyst's durability and surface-dominated reaction mechanism. Radical trapping experiments identified hydroxyl radicals ($^{\bullet}OH$) as the primary active species, generated *via* h^+-mediated H_2O oxidation and Fenton-like Fe^{3+}/Cu^{2+} redox cycles, with supplementary contributions from superoxide radicals ($^{\bullet}O_2^-$). The synergistic interplay between the Z-scheme heterojunction (enhancing light absorption and charge separation) and Fenton-like activity (amplifying ROS generation) endowed the composite with superior photocatalytic performance, achieving 99.94% MB degradation within 35 min. This work establishes $Ag_2O@CuFe_2O_4@g\text{-}C_3N_4$ as a robust, multifunctional catalyst for sustainable wastewater treatment, offering a scalable strategy to address organic pollution through solar energy utilization.

Author contributions

Jianhua Wang – funding acquisition, methodology, material synthesis, article writing, chart output, grammar correction, *etc.* Huihui Fang – material preparation, degradation experiments, grammar correction, *etc.* Shuhui Shi – project administration, supervision, grammar correction, article writing, chart output, *etc.*

Conflicts of interest

There are no conflicts to declare.

Data availability

The data supporting this article have been included as part of the supplementary information (SI). Supplementary information is available. See DOI: https://doi.org/10.1039/d5ra02882e.

Acknowledgements

The authors are thankful to lab of materials fabricated for providing experiment condition, to chemical laboratory for the

materials tests, and to Master student for carrying out the degradation experiment. This work was supported by the Joint Fund Project of Science and Technology Plan of Liaoning Province (2023-MSLH-237).

Notes and references

1 (*a*) M. S. Ahmad, K. K. Gheffar and R. Mahboubeh, *4th International Electronic Conference on Water Sciences*, 2020, vol. 48, p. 17; (*b*) Q. Qin, Y. Liu, X. Li, T. Sun and Y. Xu, *RSC Adv.*, 2018, **8**, 1071–1077; (*c*) L. Xiao, S. Gao, R. Liao, Y. Zhou, Q. Kong and G. Hu, *Mater. Horiz.*, 2024, **11**, 2545–2571; (*d*) M. Yan, Y. Wu, Y. Wu, X. Lan, J. Cheng and W. Zhao, *Mater. Horiz.*, 2024, **11**, 4438–4453.

2 (*a*) R. Cheng, X. Fan, M. Wang, M. Li, J. Tian and L. Zhang, *RSC Adv.*, 2016, **6**, 18990–18995; (*b*) Y. Yao, F. Lu, Y. Zhu, F. Wei, X. Liu, C. Lian and S. Wang, *J. Hazard. Mater.*, 2015, **297**, 224–233.

3 (*a*) Z. Cao, C. Zuo and H. Wu, *Mater. Chem. Phys.*, 2019, **237**, 121842; (*b*) T. Zhang, T. Zhou, L. He, D. Xu and L. Bai, *Synth. Met.*, 2020, **267**, 116479.

4 (*a*) L. Liu, N. Hu, Y. An, X. Du, X. Zhang, Y. Li, Y. Zeng and Z. Cui, *Materials*, 2020, **13**, 4760; (*b*) R. Hao, G. Wang, C. Jiang, H. Tang and Q. Xu, *Appl. Surf. Sci.*, 2017, **411**, 400–410; (*c*) S. R. Pattnaik, A. Behera, R. Acharya and K. Parida, *J. Environ. Chem. Eng.*, 2019, **7**, 103456.

5 (*a*) X. Guo, K. Wang, D. Li and J. Qin, *Appl. Surf. Sci.*, 2017, **420**, 792–801; (*b*) Q. Qin, Y. Liu, X. Li, T. Sun and Y. Xu, *RSC Adv.*, 2018, **8**, 1071–1077; (*c*) A. Behera, D. Kandi, S. M. Majhi, S. Martha and K. Parida, *Beilstein J. Nanotechnol.*, 2018, **9**, 436–446.

6 (*a*) S. Ghodsi, A. Esrafili, R. R. Kalantary, M. Gholami and H. R. Sobhi, *J. Photochem. Photobiol., A*, 2019, **389**, 112279; (*b*) M. S. Ahmad, K. K. Gheffar and R. Mahboubeh, *4th International Electronic Conference on Water Sciences*, 2020, vol. 48, p. 17.

7 (*a*) R. Cheng, X. Fan, M. Wang, M. Li, J. Tian and L. Zhang, *RSC Adv.*, 2016, **6**, 18990–18995; (*b*) M. Xu, L. Han and S. Dong, *ACS Appl. Mater. Interfaces*, 2013, **5**, 12533–12540; (*c*) H. Jung, T. Pham and W. Eun, *Appl. Surf. Sci.*, 2018, **458**, 369–381.

8 (*a*) J. H. Wang and W. T. Zhang, *Toxicol. Environ. Chem.*, 2023, **105**, 60–74; (*b*) J. H. Wang, *J. Phys. Chem. Solids*, 2023, **180**, 111389.

9 (*a*) T. Zhang, T. Zhou, L. He, D. Xu and L. Bai, *Synth. Met.*, 2020, **267**, 116479; (*b*) L. Liu, N. Hu, Y. An, X. Du, X. Zhang, Y. Li, Y. Zeng and Z. Cui, *Materials*, 2020, **13**, 4760.

10 (*a*) S. Ghodsi, A. Esrafili, R. R. Kalantary, M. Gholami and H. R. Sobhi, *J. Photochem. Photobiol., A*, 2019, **389**, 112279; (*b*) W. Mohammad, K. Mohamed and D. Bahnemann, *Ceram. Int.*, 2021, **47**, 31073–31083; (*c*) D. Sun, J. Mao, L. Cheng, X. Yang, H. Li, L. Zhang, W. Zhang, Q. Zhang and P. Li, *Chem. Eng. J.*, 2021, **418**, 129417.

11 (*a*) S. Ghodsi, A. Esrafili, R. R. Kalantary, M. Gholami and H. R. Sobhi, *J. Photochem. Photobiol., A*, 2019, **389**, 112279; (*b*) W. Mohammad, K. Mohamed and D. Bahnemann, *Ceram. Int.*, 2021, **47**, 31073–31083; (*c*) J. H. Wang, *J. Phys. Chem. Solids*, 2023, **180**, 111389.

12 (*a*) A. Mirzaei, Z. Chen, F. Haghighat and L. Yerushalmi, *Chemosphere*, 2018, **205**, 463–474; (*b*) S. Raha and M. Ahmaruzzaman, *Chem. Eng. J.*, 2020, **395**, 124969; (*c*) X. N. Wei and H. L. Wang, *J. Alloys Compd.*, 2018, **763**, 844–853.

13 X. N. Wei and H. L. Wang, *J. Alloys Compd.*, 2018, **763**, 844–853.

14 (*a*) Z. Cao, C. Zuo and H. Wu, *Mater. Chem. Phys.*, 2019, **237**, 121842; (*b*) M. Xu, L. Han and S. Dong, *ACS Appl. Mater. Interfaces*, 2013, **5**, 12533–12540.

15 (*a*) L. Liu, N. Hu, Y. An, X. Du, X. Zhang, Y. Li, Y. Zeng and Z. Cui, *Materials*, 2020, **13**, 4760; (*b*) W. Mohammad, K. Mohamed and D. Bahnemann, *Ceram. Int.*, 2021, **47**, 31073–31083.

16 (*a*) S. Kamal, S. Balu, S. Palanisamy, K. Uma, V. Velusamy and T. C. K. Yang, *Results Phys.*, 2019, **12**, 1238–1244; (*b*) H. Chen, L. Qiu, J. Xiao, S. Ye, X. Jiang and Y. Yuan, *RSC Adv.*, 2014, **4**, 22491–22496; (*c*) S. Zhang, C. Su, H. Ren, M. Li, L. Zhu, S. Ge, M. Wang, Z. Zhang, L. Li and X. Cao, *Nanomaterials*, 2019, **9**, 215; (*d*) S. Vadivel, D. Maruthamani, A. Habibi-Yangjeh, B. Paul, S. Sankar Dhar and K. Selvam, *J. Colloid Interface Sci.*, 2016, **480**, 126–136; (*e*) Q. Fang, B. Li, Y. Li, W. Huang, W. Peng, X. Fan and G. Huang, *Adv. Powder Technol.*, 2019, **30**, 1576–1583; (*f*) X. Guo, K. Wang, D. Li and J. Qin, *Appl. Surf. Sci.*, 2017, **420**, 792–801.

17 A. Ghosh and A. Zubair, *Surf. Interfaces*, 2024, **55**, 105397.

18 R. Shahriar, K. S. Hoque and A. Zubair, *Catal. Sci. Technol.*, 2023, **13**, 1164–1172.